symmetry

MDPI

Article

Startup of Couette Flow and the Rayleigh–Stokes Problem in a Right-Angled Isosceles Triangular Channel

Vinícius Coutinho da Silva and André von Borries Lopes *

Departamento de Engenharia Mecânica, Faculdade de Tecnologia, Universidade de Brasília, Brasília 70910-900, DF, Brazil; viniciuscoutinho04@gmail.com
* Correspondence: andre.lopes@unb.br

Abstract

Exact solutions of the Navier–Stokes equations are derived for three startup flows in a right-angled isosceles triangular channel: Couette flow driven by impulsive motion of the hypotenuse, Couette flow driven by impulsive motion of one leg, and the Rayleigh–Stokes problem with all three walls set simultaneously into motion. Explicit transient series are obtained for the velocity field, the volumetric flow rate, and the net viscous momentum transfer. These solutions show how the triangular geometry modifies the transient response and the wall loading, and they provide exact benchmarks for startup flows in a non-separable domain.

Keywords: Couette flow; exact solution; Navier–Stokes equations; Rayleigh–Stokes problem; triangular channel; unsteady flow

1. Introduction

The Rayleigh–Stokes problem (also known as Stokes' first problem) concerns the unsteady motion in a semi-infinite viscous fluid set into motion by a flat plate suddenly moving at constant velocity. It is a canonical example of momentum diffusion and transient boundary-layer formation: the velocity satisfies the one-dimensional heat equation and evolves in a self-similar profile. Stokes first derived the solution in 1851 while studying internal fluid friction and pendulum motion [1], and Rayleigh later revisited it in the broader context of unsteady viscous flow past solid boundaries [2].

If the fluid is instead confined between two parallel plates, and one of them is impulsively set into motion with constant velocity while the other remains fixed, the flow exhibits a distinct character. The presence of the stationary wall inhibits self-similar development and constrains the diffusion of momentum. The velocity field evolves toward the steady linear Couette profile. This is the startup problem for plane Couette flow [3].

There is a broad literature on extensions of the Rayleigh–Stokes and startup Couette problems. In the Rayleigh–Stokes setting, periodic wall motion leads to Stokes' second problem, first treated by Stokes [1]. Stewartson [4] analysed the unsteady boundary layer induced by an impulsively started semi-infinite plate, while MacDonald [5] treated two immiscible layers. Tanner [6], Fetecau and Fetecau [7], and Preziosi and Joseph [8] developed viscoelastic generalisations using Oldroyd-B and Boltzmann-type models. Recent work has revisited Stokes' second problem under non-trivial thermal boundary conditions, obtaining closed-form velocity fields and quantifying the associated heat-transfer response [9]. Exact Rayleigh–Stokes solutions have also been reported for viscoelastic models in more elaborate settings, such as a Maxwell fluid in a porous medium and a rotating frame,

Check for updates

Received: 4 February 2026
Revised: 23 March 2026
Accepted: 27 March 2026
Published: 16 July 2026

Copyright: © 2026 by the authors. Licensee MDPI, Basel, Switzerland. This article is an open access article distributed under the terms and conditions of the Creative Commons Attribution (CC BY) license.

obtained by Laplace and Fourier techniques [10]. For startup Couette flow, Erdoğan [11] examined symmetric motion of both plates; Bandelli and Rajagopal [12] obtained exact solutions for second-grade fluids; Wenchang, Wenxiao, and Mingyu [13] treated a fractional Maxwell fluid; Vieru and Zafar [14] studied Maxwell fluids with wall slip; and Jordan and Puri [15] analysed a second-grade Rivlin–Ericksen fluid in a porous half-space. Further contributions include numerical modelling of viscoelastic startup flows [16] and variable-viscosity effects in unsteady Couette flow [17]. More broadly, viscous flows driven by non-uniform wall motion, including stretching-surface boundary-layer configurations, have also been studied in the literature [18–21]. This list is not exhaustive.

Beyond the semi-infinite setting, related startup mechanisms have also been analysed for exterior-cylinder flows and for closed geometries. Wu and Wu [22] formulated a generalised Rayleigh problem for an infinitely long cylinder of arbitrary cross-section set impulsively into axial motion, developing small- and large-time analyses and integral representations, with the circular cylinder presented as a reference case. Erdoğan [23] presented exact unsteady solutions generated by a sudden application of a constant pressure gradient or by the impulsive motion of a boundary in canonical closed configurations, including circular and rectangular channels and a rotating cylinder, and derived series for the velocity, flux, and wall shear at short and long times. More recently, da Silva et al. [24] obtained exact startup solutions for pressure-driven flow in triangular ducts, including hemi-equilateral and right-angled isosceles cross-sections. Their study is complementary to the present one, since the startup there was driven by an imposed pressure gradient, whereas here it is generated by impulsive wall motion. In the non-Newtonian setting, Nadeem et al. [25] treated the Rayleigh–Stokes startup in a rectangular pipe for Maxwell and second-grade fluids. Xia et al. [26] proposed a Laplace–eigenfunction framework for Couette flow of generalised linear viscoelastic fluids in non-circular sections and obtained an analytical startup solution for a rectangular pipe with a generalised Burgers fluid. Further recent contributions have extended Rayleigh–Stokes and startup Couette-type formulations to fractional and non-local-in-time models, rigorous well-posedness theory, and high-accuracy numerical schemes, including the mixed nonlinear time-fractional Rayleigh–Stokes equation studied by Au and Caraballo [27], semilinear fractional Rayleigh–Stokes problems on unbounded domains analysed by He [28], non-local fractional Rayleigh–Stokes equations treated by Ashurov et al. [29], fast spectral and Galerkin approximations developed by Long et al. [30] and Abd-Elhameed et al. [31], and mesh-free techniques for inverse fractional Rayleigh–Stokes models proposed by Safari and Feng [32].

The aim of this work is to obtain exact analytical solutions for the startup flow of an incompressible Newtonian fluid in a right-angled isosceles triangular channel. The problem is viewed as a canonical benchmark for transient momentum diffusion in a non-circular channel, rather than as a detailed model of a particular engineering device. Three configurations are studied: impulsive motion of the hypotenuse, impulsive motion of one leg, and the Rayleigh–Stokes case in which all three walls move simultaneously.

After Laplace transformation in time, each configuration reduces to a Helmholtz problem in the triangular cross-section with non-homogeneous Dirichlet boundary data. Problems of the Helmholtz type arise in a wide range of settings, including fluid mechanics [33–35], acoustic and electromagnetic wave propagation [36,37], transient heat conduction [38,39], and water waves [40–42]. However, explicit spectral constructions are usually confined to geometries that admit separable coordinates, such as rectangles, circles, and annuli [43]. For non-orthogonal domains, including triangles and irregular polygons, analytical treatments are considerably more delicate and are often replaced by numerical approximations. The right-angled isosceles triangle considered here is a notable exception: although non-separable in its physical form, it possesses enough symmetry to

permit explicit spectral constructions after suitable reflection and coordinate transformation. By exploiting these symmetries, one can derive explicit transient series for the velocity field and the volumetric flow rate.

The novelty of the present study lies in three points: First, we obtain exact transient solutions for three impulsively driven startup flows in a closed right-angled isosceles triangular channel. Secondly, we show how the symmetry of the domain can be used to reduce the original problems to separable Helmholtz problems and thereby construct explicit eigenfunction expansions. Thirdly, we derive not only the velocity field but also explicit expressions for the volumetric flow rate and the net viscous momentum transfer, together with their short- and long-time asymptotics. The analysis also makes clear the difference between the compatible Rayleigh–Stokes configuration, for which the wall loads remain finite for $t > 0$, and the impulsively started Couette configurations, for which corner singularities are present.

This work is organised as follows: Section 2 formulates the problem, including the governing equations, boundary conditions, and non-dimensionalisation. Section 3 derives the analytical solution for startup Couette flow in two configurations and examines the corresponding velocity contours. Section 4 treats the Rayleigh–Stokes problem, giving its analytical solution and discussing the transient behaviour. Section 5 compares the present results with classical exact startup solutions in square and circular geometries. Finally, Section 6 summarises the main findings and indicates directions for future work.

2. Formulation

Consider a channel of right-angled isosceles triangular cross-section, with hypotenuse of length $2L$, containing a Newtonian fluid of kinematic viscosity ν, initially at rest. The corresponding legs have length $\sqrt{2}L$, so that the geometry is unique up to an overall scaling. Three classical unsteady problems are considered: (i) two Couette-type startup flows, in which either the wall along the hypotenuse or the wall along the right leg (i.e., the one aligned with $y = x$) suddenly begins to move at constant velocity V in the axial direction at $t = 0$, while the remaining walls are held fixed; and (ii) the Rayleigh–Stokes problem, in which all three walls simultaneously start moving in the same direction with velocity V. All lengths are non-dimensionalised by L, velocity by V, and time by L^2/ν. The adopted Cartesian coordinate system is shown in Figure 1.

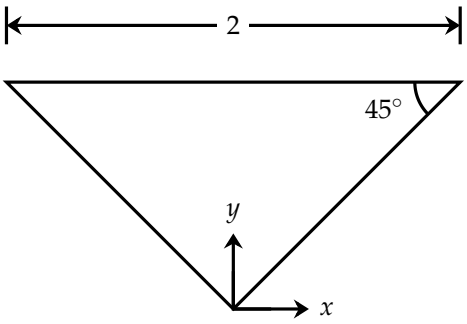


Figure 1. Cross-section of a right-angled isosceles triangular channel.

We consider the standard framework of unsteady rectilinear motion of an incompressible Newtonian fluid, with a single non-zero axial velocity component $w(x, y, t)$ and no imposed axial pressure gradient (see, e.g., Papanastasiou, Georgiou, and Alexandrou [3]). Under these assumptions, the incompressible Navier–Stokes equations reduce to the heat equation

$$\frac{\partial w}{\partial t} = \nabla^2 w, \tag{1}$$

where $w(x, y, t)$ is the velocity in the axial direction.

For flow driven by the wall along the hypotenuse,

$$\begin{cases} w(x, y = x, t) = 0, \\ w(x, y = -x, t) = 0, \\ w(x, y = 1, t) = 1, \end{cases} \tag{2}$$

and for flow driven by the wall along the right leg,

$$\begin{cases} w(x, y = x, t) = 1, \\ w(x, y = -x, t) = 0, \\ w(x, y = 1, t) = 0, \end{cases} \tag{3}$$

For the Rayleigh–Stokes flow,

$$\begin{cases} w(x, y = x, t) = 1, \\ w(x, y = -x, t) = 1, \\ w(x, y = 1, t) = 1, \end{cases} \tag{4}$$

and in all cases,

$$w(x, y, t = 0) = 0. \tag{5}$$

Because the wall motion is imposed impulsively, the initial condition and the boundary data are incompatible at $t = 0$ on each moving wall. The series solutions are therefore to be interpreted for $t > 0$, rather than by termwise evaluation at $t = 0$. For every fixed $t > 0$, the parabolic character of the governing equation smooths the interior field, whereas the limit $t \to 0^+$ is non-uniform: the fluid remains close to rest away from the boundaries, while thin startup boundary layers of thickness $O\left(t^{1/2}\right)$ develop adjacent to the moving walls. Thus, the relevant short-time issue is not a persistent Gibbs phenomenon for $t > 0$, but the singular initial layer generated by the impulsive start.

To characterise the viscous loading on the walls, let $\partial/\partial n$ denote differentiation along the outward unit normal. The corresponding dimensionless wall shear tractions, scaled by $\mu V/L$, are

$$\tau_{y=1}(x, t) = -\frac{\partial w}{\partial n} = -\left.\frac{\partial w}{\partial y}\right|_{y=1}, \tag{6a}$$

$$\tau_{y=x}(x, t) = -\frac{\partial w}{\partial n} = -\frac{1}{\sqrt{2}}\left.\left(\frac{\partial w}{\partial x} - \frac{\partial w}{\partial y}\right)\right|_{y=x}, \tag{6b}$$

$$\tau_{y=-x}(x, t) = -\frac{\partial w}{\partial n} = \frac{1}{\sqrt{2}}\left.\left(\frac{\partial w}{\partial x} + \frac{\partial w}{\partial y}\right)\right|_{y=-x}, \tag{6c}$$

corresponding respectively to the hypotenuse, the right leg, and the left leg. The associated resultant forces are obtained by integrating these tractions along each side. In the Couette configurations, however, these integrals are singular because the boundary data are incompatible at the vertices where a moving wall meets a stationary one. By contrast, in the Rayleigh–Stokes problem, the boundary data are compatible on all three sides, and the corresponding resultant wall forces are finite for every $t > 0$.

Since the dimensionless volumetric flow rate is

$$Q(t) = \int_{-1}^{1} \int_{|x|}^{1} w(x, y, t)\, \mathrm{d}y\, \mathrm{d}x, \tag{7}$$

differentiation of (7), followed by the use of (1) and the divergence theorem, yields

$$\begin{aligned}\frac{\mathrm{d}Q}{\mathrm{d}t} &= \int_{-1}^{1}\int_{|x|}^{1}\frac{\partial w}{\partial t}\,\mathrm{d}y\,\mathrm{d}x \\ &= \int_{-1}^{1}\int_{|x|}^{1}\nabla^2 w\,\mathrm{d}y\,\mathrm{d}x \\ &= \int_{y=1}\frac{\partial w}{\partial n}\,\mathrm{d}s + \int_{y=x}\frac{\partial w}{\partial n}\,\mathrm{d}s + \int_{y=-x}\frac{\partial w}{\partial n}\,\mathrm{d}s.\end{aligned} \tag{8}$$

Accordingly, we define

$$F(t) = \frac{\mathrm{d}Q}{\mathrm{d}t} \tag{9}$$

as the net rate of viscous momentum transfer from the boundary to the fluid. For the impulsively started Couette problems, $F(t)$ is finite for every $t > 0$ but becomes singular as $t \to 0^+$. However, the resultant force on each individual wall is singular for all $t > 0$, owing to the incompatibility of the boundary data at the vertices where moving and stationary walls meet. In the Rayleigh–Stokes problem, by contrast, the boundary data are compatible on all three sides, so the resultant force on each wall remains finite for every $t > 0$, although the impulsive start still produces a short-time singularity in $F(t)$ as $t \to 0^+$.

3. Startup of Couette Flow

3.1. Moving Wall Along the Hypotenuse

To solve the problem analytically, we introduce an auxiliary extension from the triangular domain $\{(x, y) \in \mathbb{R}^2 : |x| < y < 1\}$ to the square $[-1, 1]^2$. This extension is not a new physical flow problem but an auxiliary construction based on odd reflection across the stationary walls $y = x$ and $y = -x$, on which the original solution vanishes. Since the boundary condition is homogeneous on these two sides, odd reflection preserves both the heat equation and the zero value on the reflecting line. In particular, reflecting the moving side $y = 1$, where $w = 1$, across either stationary leg produces the image value $w = -1$ on the corresponding vertical side of the square, while reflecting across both legs produces the value $w = 1$ on $y = -1$. Thus, the values ± 1 prescribed on the boundary of the square are image values generated by the reflection procedure, not additional physical wall velocities. The physical solution of the original startup problem is recovered by restricting the extended solution back to the triangular domain. The corresponding boundary conditions in the square are therefore

$$\begin{cases} w(x = -1, y, t) = -1, \\ w(x = 1, y, t) = -1, \\ w(x, y = -1, t) = 1, \\ w(x, y = 1, t) = 1. \end{cases} \tag{10}$$

This formulation is more convenient for obtaining an analytical solution, as shown below.

Taking the Laplace transform with respect to t in Equations (1) and (10), and using the initial condition (5), we obtain

$$\frac{\partial^2 W}{\partial x^2} + \frac{\partial^2 W}{\partial y^2} - sW = 0, \tag{11}$$

$$\begin{cases} W(x = -1, y, s) = -\dfrac{1}{s}, \\ W(x = 1, y, s) = -\dfrac{1}{s}, \\ W(x, y = -1, s) = \dfrac{1}{s}, \\ W(x, y = 1, s) = \dfrac{1}{s}, \end{cases} \tag{12}$$

where

$$W(x,y,s) = \mathscr{L}\{w(x,y,t)\} = \int_0^\infty w(x,y,t)\,\mathrm{e}^{-st}\,\mathrm{d}t, \tag{13}$$

where s is the Laplace parameter. Equation (11) is a Helmholtz equation. By separation of variables in rectangular coordinates (see, e.g., Ref. [44]), the solution subject to (12) is

$$\begin{aligned} W(x,y,s) = 2\sum_{m=1}^{\infty} \frac{\sin(\alpha_m(1+x))\cosh\left(\sqrt{s+\alpha_m^2}\,y\right)}{s\alpha_m\cosh\left(\sqrt{s+\alpha_m^2}\right)} \\ - 2\sum_{m=1}^{\infty} \frac{\cosh\left(\sqrt{s+\alpha_m^2}\,x\right)\sin(\alpha_m(1+y))}{s\alpha_m\cosh\left(\sqrt{s+\alpha_m^2}\right)}, \end{aligned} \tag{14}$$

where

$$\alpha_m = \frac{(2m-1)\pi}{2}. \tag{15}$$

The inverse Laplace transform gives

$$\begin{aligned} w(x,y,t) = 2\sum_{m=1}^{\infty} \frac{\sin(\alpha_m(1+x))}{\alpha_m}\mathscr{L}^{-1}\left\{\frac{\cosh\left(\sqrt{s+\alpha_m^2}\,y\right)}{s\cosh\left(\sqrt{s+\alpha_m^2}\right)}\right\} \\ - 2\sum_{m=1}^{\infty} \frac{\sin(\alpha_m(1+y))}{\alpha_m}\mathscr{L}^{-1}\left\{\frac{\cosh\left(\sqrt{s+\alpha_m^2}\,x\right)}{s\cosh\left(\sqrt{s+\alpha_m^2}\right)}\right\}. \end{aligned} \tag{16}$$

By applying Cauchy's residue theorem, we find that

$$\begin{aligned} w(x,y,t) = 2\sum_{m=1}^{\infty} \frac{\sin(\alpha_m(1+x))\cosh(\alpha_m y)}{\alpha_m\cosh(\alpha_m)} - 2\sum_{m=1}^{\infty} \frac{\sin(\alpha_m(1+y))\cosh(\alpha_m x)}{\alpha_m\cosh(\alpha_m)} \\ + 4\sum_{m=1}^{\infty}\sum_{n=1}^{\infty} \frac{(-1)^n\alpha_n}{\alpha_m(\alpha_m^2+\alpha_n^2)}\sin(\alpha_m(1+x))\cos(\alpha_n y)\mathrm{e}^{-(\alpha_m^2+\alpha_n^2)t} \\ - 4\sum_{m=1}^{\infty}\sum_{n=1}^{\infty} \frac{(-1)^n\alpha_n}{\alpha_m(\alpha_m^2+\alpha_n^2)}\sin(\alpha_m(1+y))\cos(\alpha_n x)\mathrm{e}^{-(\alpha_m^2+\alpha_n^2)t}. \end{aligned} \tag{17}$$

For each fixed $t > 0$, the exponential factors in (17) ensure rapid convergence of the transient part of the double series, so that the representation is well defined pointwise in the triangular interior. The limit $t \to 0^+$, however, is non-uniform: the interior field tends to the quiescent initial state, whereas the moving hypotenuse retains the value $w = 1$. This mismatch is resolved through a thin startup boundary layer adjacent to the moving wall. At the vertices $(\pm 1, 1)$, where the moving and stationary walls meet, the local gradients become singular, consistent with the divergent wall tractions discussed in Section 2.

The velocity contours for the startup Couette flow are shown in Figure 2 for $t = 0.02$, 0.06, and 0.1, arranged from top to bottom. The contours range from 0 to 1 in increments of 0.1, with the maximum dimensionless velocity occurring along the moving boundary, where the hypotenuse is impulsively set into motion.

As time progresses, the velocity field evolves from a thin boundary layer near the hypotenuse ($t = 0.02$) to a more developed flow with broader diffusion into the triangular domain. At early times ($t = 0.02$), the influence of the impulsive motion is confined near the moving wall, and the interior remains mostly stagnant. At $t = 0.06$, the contours begin to spread more deeply into the domain, indicating the development of shear layers. Finally, by $t = 0.1$, the velocity field becomes well established across the domain, with the flow profile already close to the steady state.

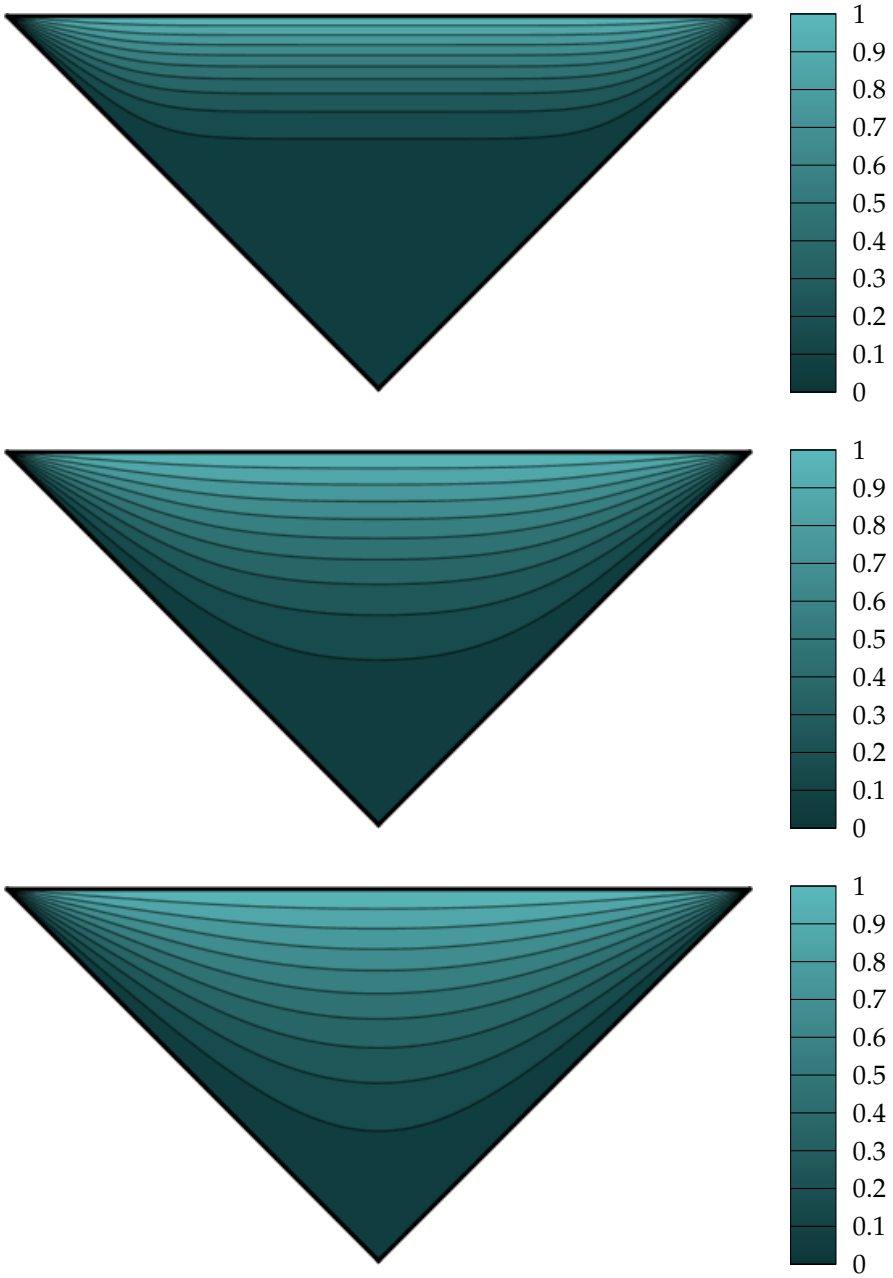


Figure 2. Velocity contours for the startup of Couette flow in a right-angled isosceles triangular channel, with the moving wall along the hypotenuse, at $t = 0.02$, 0.06, and 0.1 (from top to bottom).

The volumetric flow rate is given by

$$\begin{aligned} Q(t) &= \int_{-1}^{1} \int_{|x|}^{1} w(x,y,t)\,\mathrm{d}y\,\mathrm{d}x \\ &= -4\sum_{m=1}^{\infty} \frac{(-1)^m}{\alpha_m^3 \cosh(\alpha_m)} - 4\sum_{m=1}^{\infty}\sum_{n=1}^{\infty} \frac{[\alpha_m(-1)^m - \alpha_n(-1)^n]^2}{\alpha_m^2\alpha_n^2(\alpha_m^2+\alpha_n^2)} \mathrm{e}^{-(\alpha_m^2+\alpha_n^2)t}, \end{aligned} \tag{18}$$

from which it follows that

$$Q_\infty = \lim_{t\to\infty} Q(t) = -4\sum_{m=1}^{\infty} \frac{(-1)^m}{\alpha_m^3 \cosh(\alpha_m)} \approx 0.4106. \tag{19}$$

The second term in Equation (18) represents the transient response. At short times, the flow is confined to a thin viscous layer adjacent to the moving wall, and the solution

is locally described by the classical Stokes' first problem in a half-plane. Accordingly, the flux contribution is $2\sqrt{t/\pi}$ per unit wall length. Since the hypotenuse has a length of 2, one obtains

$$Q(t) \sim \frac{4}{\sqrt{\pi}}\, t^{1/2}, \quad t \to 0^{+}, \tag{20}$$

which reflects the local penetration of vorticity from the moving wall into the fluid. At long times, the transient is governed by the first non-vanishing term in the double series, corresponding to $(m, n) = (1, 2)$ and $(2, 1)$, so that

$$Q_{\infty} - Q(t) \sim \frac{1024}{45\pi^4} \mathrm{e}^{-\frac{5\pi^2}{2}t}, \quad t \to \infty. \tag{21}$$

Thus, the startup process crosses over from an early diffusive regime to a late exponential relaxation governed by the slowest-decaying eigenmode.

At $t = 0.001$, the volumetric flow rate is about 17% of its steady-state value, as shown in Figure 3. This indicates a rapid initial transfer of momentum from the moving wall into the fluid. The subsequent evolution is slower, and the volumetric flow rate reaches about 95% of its steady-state value at $t \approx 0.1$. Figure 3 also shows that the exact solution is well described by the asymptotic approximations (20) and (21) in the corresponding early- and late-time regimes.

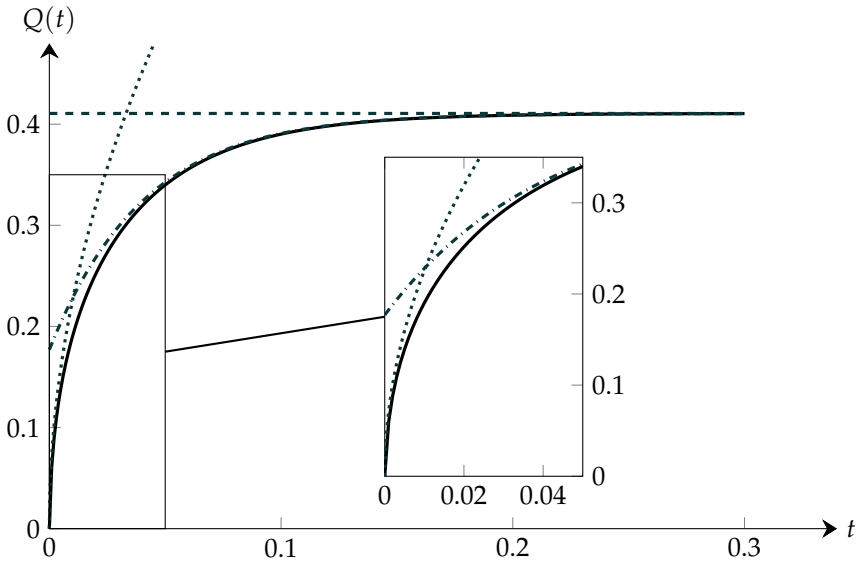


Figure 3. Volumetric flow rate, $Q(t)$, for the startup of Couette flow in a right-angled isosceles triangular channel, with the moving wall along the hypotenuse. The solid curve represents the exact solution, the dashed horizontal line indicates the steady-state limit, the dotted curve shows the short-time asymptotic approximation, and the dash-dotted curve shows the long-time asymptotic approximation.

To examine the numerical convergence of (18), Table 1 lists the values of $Q(t)$ obtained by truncating the first series at $m = 1, \ldots, N$ and the double series at $m, n = 1, \ldots, N$, for $N = 1, 2, 4, 8$, and 16. The convergence is rapid for all three times considered. The value corresponding to $N = 1$ is the same for every t because the term $(m, n) = (1, 1)$ in the transient double series vanishes identically, so that this truncation retains only the leading contribution from the steady part. Once $N = 2$ is included, the transient correction becomes active and the approximation moves towards the converged value. For $t = 0.1$, the reported digits are already recovered with $N = 4$, whereas for $t = 0.02$ and $t = 0.06$ one needs $N = 8$.

Table 1. Convergence of the truncated volumetric flow rate, $Q(t)$, for startup Couette flow in a right-angled isosceles triangular channel, with the moving wall along the hypotenuse. A dash indicates that the value has converged.

t/N	1	2	4	8	16
0.02	0.41130956	0.26800556	0.25398045	0.25368904	–
0.06	0.41130956	0.35746828	0.35669293	0.35669286	–
0.1	0.41130956	0.39081173	0.39076246	–	–

Finally, from (9) and (18), the net rate of viscous momentum transfer from the boundary to the fluid is

$$F(t) = 4 \sum_{m=1}^{\infty} \sum_{n=1}^{\infty} \frac{[\alpha_m(-1)^m - \alpha_n(-1)^n]^2}{\alpha_m^2 \alpha_n^2} \mathrm{e}^{-\left(\alpha_m^2 + \alpha_n^2\right)t}. \tag{22}$$

Figure 4 shows that this quantity is concentrated near startup and then decays monotonically to zero. Its magnitude is initially $O(1)$, falls below unity in the transient, and is already $O(10^{-2})$ by $t = O(10^{-1})$. Thus, most of the viscous loading is transmitted during the early stage of the motion, after which the load becomes negligible as the flow approaches its steady Couette state.

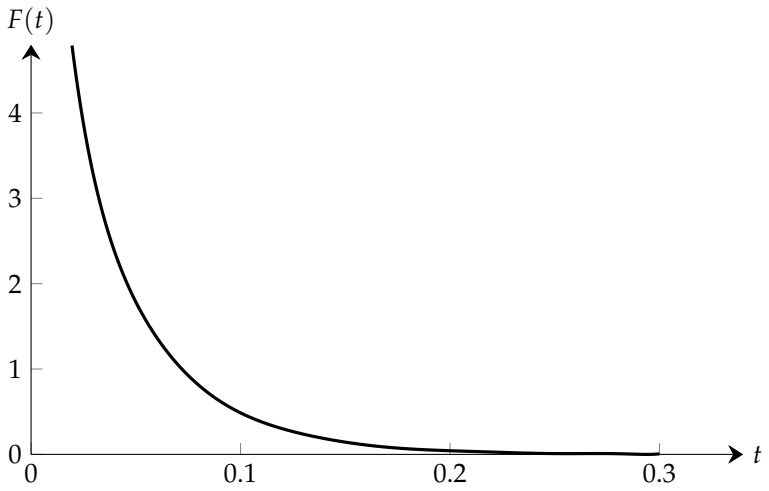


Figure 4. Net rate of viscous momentum transfer from the boundary to the fluid, $F(t)$, for the startup of Couette flow in a right-angled isosceles triangular channel, with the moving wall along the hypotenuse.

3.2. Moving Wall Along the Right Leg

To simplify the problem, we introduce the change in variables

$$x' = \frac{x+y}{2}, \quad y' = \frac{y-x}{2}, \quad t' = \frac{t}{2}, \tag{23}$$

which corresponds to a 45° clockwise rotation, followed by a rescaling of space and time. Under this transformation, the triangular domain $\{(x,y) \in \mathbb{R}^2 : |x| < y < 1\}$ is mapped onto the unit right triangle $\{(x',y') \in \mathbb{R}^2 : x' > 0,\ y' > 0,\ x' + y' < 1\}$, whose legs are aligned with the coordinate axes. More precisely, the boundaries $y = -x$, $y = x$, and $y = 1$ are mapped onto $x' = 0$, $y' = 0$, and $x' + y' = 1$, respectively. Thus, the moving wall and the fixed walls are naturally transferred to the sides of the transformed triangle.

In these variables, the heat Equation (1) becomes

$$\frac{\partial w}{\partial t'} = \frac{\partial^2 w}{\partial x'^2} + \frac{\partial^2 w}{\partial y'^2}. \tag{24}$$

The boundary conditions (3) take the form

$$\begin{cases} w(x'=0,y',t')=0, \\ w(x',y'=0,t')=1, \\ w(x',y'=1-x',t')=0, \end{cases} \tag{25}$$

with

$$w(x',y',0)=0 \tag{26}$$

as the initial condition.

As before, we extend the problem from the unit right triangle to the square $\{(x',y')\in[0,1]^2\}$ by antisymmetry with respect to the diagonal $x'+y'=1$, which is left fixed by the reflection $(x',y')\mapsto(1-y',1-x')$. This extension preserves the condition on the hypotenuse and allows for the separation of variables in the square. The corresponding boundary conditions are

$$\begin{cases} w(x'=0,y',t')=0, \\ w(x'=1,y',t')=-1, \\ w(x',y'=0,t')=1, \\ w(x',y'=1,t')=0. \end{cases} \tag{27}$$

Applying the Laplace transform in time to Equation (24), with the initial condition (26), yields

$$\frac{\partial^2 W}{\partial x'^2}+\frac{\partial^2 W}{\partial y'^2}-sW=0, \tag{28}$$

where

$$W(x',y',s)=\mathscr{L}\{w(x',y',t')\}=\int_0^\infty w(x',y',t')\,\mathrm{e}^{-st'}\,\mathrm{d}t'. \tag{29}$$

The boundary conditions for W follow from (27) and read

$$\begin{cases} W(x'=0,y',s)=0, \\ W(x'=1,y',s)=-\dfrac{1}{s}, \\ W(x',y'=0,s)=\dfrac{1}{s}, \\ W(x',y'=1,s)=0. \end{cases} \tag{30}$$

Solving the Helmholtz Equation (28) subject to the boundary conditions (30), we obtain

$$\begin{aligned} W(x',y',s)=2\sum_{m=1}^{\infty}\sin(2\alpha_m x')\,\frac{\sinh\left(\sqrt{s+4\alpha_m^2}\,(1-y')\right)}{s\alpha_m\sinh\left(\sqrt{s+4\alpha_m^2}\right)} \\ -2\sum_{m=1}^{\infty}\frac{\sin(2\alpha_m y')\sinh\left(\sqrt{s+4\alpha_m^2}\,x'\right)}{s\alpha_m\sinh\left(\sqrt{s+4\alpha_m^2}\right)}. \end{aligned} \tag{31}$$

See also Ref. [44]. The inverse Laplace transform yields

$$\begin{aligned} w(x',y',t')=2\sum_{m=1}^{\infty}\frac{\sin(2\alpha_m x')}{\alpha_m}\mathscr{L}^{-1}\left\{\frac{\sinh\left(\sqrt{s+4\alpha_m^2}\,(1-y')\right)}{s\sinh\left(\sqrt{s+4\alpha_m^2}\right)}\right\} \\ -2\sum_{m=1}^{\infty}\frac{\sin(2\alpha_m y')}{\alpha_m}\mathscr{L}^{-1}\left\{\frac{\sinh\left(\sqrt{s+4\alpha_m^2}\,x'\right)}{s\sinh\left(\sqrt{s+4\alpha_m^2}\right)}\right\}. \end{aligned} \tag{32}$$

Using Cauchy's residue theorem, it follows that

$$\begin{aligned} w(x',y',t') = 2\sum_{m=1}^{\infty}\frac{\sin(2\alpha_m x')\sinh(2\alpha_m(1-y'))}{\alpha_m\sinh(2\alpha_m)} - 2\sum_{m=1}^{\infty}\frac{\sin(2\alpha_m y')\sinh(2\alpha_m x')}{\alpha_m\sinh(2\alpha_m)} \\ + 4\sum_{m=1}^{\infty}\sum_{n=1}^{\infty}\frac{(-1)^n\beta_n}{\alpha_m(4\alpha_m^2+\beta_n^2)}\sin(2\alpha_m x')\sin(\beta_n(1-y'))\mathrm{e}^{-(4\alpha_m^2+\beta_n^2)t'} \\ - 4\sum_{m=1}^{\infty}\sum_{n=1}^{\infty}\frac{(-1)^n\beta_n}{\alpha_m(4\alpha_m^2+\beta_n^2)}\sin(2\alpha_m y')\sin(\beta_n x')\mathrm{e}^{-(4\alpha_m^2+\beta_n^2)t'}. \end{aligned} \tag{33}$$

where

$$\beta_n = n\pi. \tag{34}$$

The same interpretation applies here. For every fixed $t' > 0$, the series in (33) converges rapidly and represents the physical solution in the triangular domain. As $t' \to 0^+$, the limit is again non-uniform because the fluid is initially at rest, whereas the wall $y' = 0$ is set instantaneously to unit velocity. The resulting short-time structure is a startup boundary layer adjacent to the moving leg, together with singular corner behaviour at the vertices where moving and stationary walls meet.

Figure 5 shows normalised velocity contours for the startup of Couette flow when the impulsive motion is applied along the right leg. The panels correspond to $t = 0.02$, 0.06, and 0.1, from top to bottom. Contours run from 0 to 1 in increments of 0.1, with the maximum located along the moving wall.

At early times ($t = 0.02$), the influence of the wall motion remains confined to a narrow region adjacent to the right leg, with a steep velocity gradient, while the remainder of the domain is nearly quiescent. As time progresses, viscous diffusion drives the flow further into the triangular domain. By $t = 0.1$, the velocity field has spread significantly and is already close to the steady state, although much of the fluid near the left leg still experiences low velocities. Compared to the case where the hypotenuse is in motion, the present configuration results in a more localised development of the flow.

The volumetric flow rate follows upon integration over the triangular cross-section:

$$Q(t) = \sum_{m=1}^{\infty}\frac{\coth(\alpha_m)}{\alpha_m^3} + 16\sum_{m=1}^{\infty}\sum_{n=1}^{\infty}\frac{\beta_{2n}^2}{\alpha_m^2(16\alpha_m^4-\beta_{2n}^4)}\mathrm{e}^{-\frac{4\alpha_m^2+\beta_{2n}^2}{2}t}. \tag{35}$$

Since only the even Fourier modes contribute after integration, the slowest-decaying term corresponds to $m = 1$ and β_2. It follows from (35) that

$$Q_\infty = \lim_{t\to\infty} Q(t) = \sum_{m=1}^{\infty}\frac{\coth(\alpha_m)}{\alpha_m^3} \approx 0.2947. \tag{36}$$

The behaviour of $Q(t)$ is also simple in the limits $t \to 0^+$ and $t \to \infty$. As $t \to 0^+$, the motion is confined to a thin layer adjacent to the moving leg, and the local behaviour is again that of Stokes' first problem. Since the associated flux contribution is $2\sqrt{t/\pi}$ per unit wall length, and since the moving boundary has length $\sqrt{2}$, we obtain

$$Q(t) \sim 2\sqrt{\frac{2}{\pi}}\,t^{1/2}, \quad t \to 0^+. \tag{37}$$

Thus, the initial growth of $Q(t)$ is diffusive, although it is weaker than in the hypotenuse-driven case. As $t \to \infty$, the transient is governed by the leading term in (35), namely, $m = 1$ and $n = 1$; therefore,

$$Q_\infty - Q(t) \sim \frac{256}{15\pi^4}\mathrm{e}^{-\frac{5\pi^2}{2}t}, \quad t \to \infty. \tag{38}$$

The approach to the steady state is therefore exponential, with the same decay rate as in the hypotenuse-driven case, but with a smaller prefactor. The time evolution of $Q(t)$ for this configuration is shown in Figure 6.

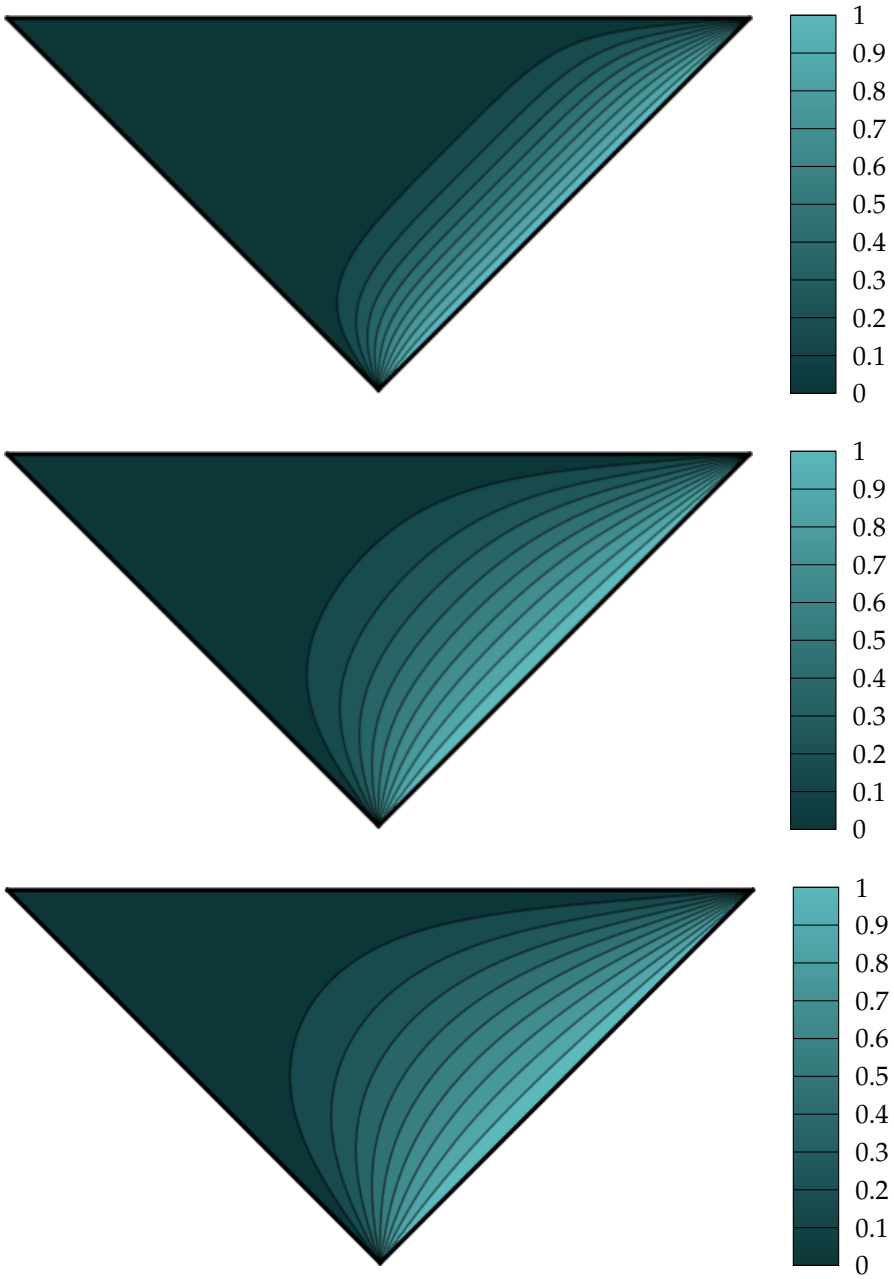


Figure 5. Velocity contours for the startup of Couette flow in a right-angled isosceles triangular channel, with the moving wall along the right leg, at $t = 0.02$, 0.06, and 0.1 (from top to bottom).

The convergence in Table 2 is slower than in Table 1. For $t = 0.06$ and $t = 0.1$, the reported digits are recovered with $N = 16$, whereas for $t = 0.02$ one needs $N = 32$. This is consistent with the weaker exponential damping at earlier times, when a larger number of modes still contributes appreciably.

From (9) and (35), the net rate of viscous momentum transfer from the boundary to the fluid is

$$F(t) = 8 \sum_{m=1}^{\infty} \sum_{n=1}^{\infty} \frac{\beta_{2n}^2}{\alpha_m^2 \left(\beta_{2n}^2 - 4\alpha_m^2\right)} \mathrm{e}^{-\frac{4\alpha_m^2 + \beta_{2n}^2}{2} t}. \tag{39}$$

Figure 7 shows that, as in the hypotenuse-driven case, $F(t)$ attains its largest values near startup and then decays monotonically to zero. The same qualitative behaviour is therefore preserved, but at a lower overall level in the present configuration, because the moving boundary is shorter.

Table 2. Convergence of the truncated volumetric flow rate, $Q(t)$, for startup Couette flow in a right-angled isosceles triangular channel, with the moving wall along one leg. A dash indicates that the value has converged.

t/N	1	2	4	8	16	32	64
0.02	0.1744	0.1769	0.1792	0.1800	0.1801	0.1802	–
0.06	0.2415	0.2508	0.2536	0.2544	0.2546	–	–
0.1	0.2665	0.2760	0.2788	0.2796	0.2798	–	–

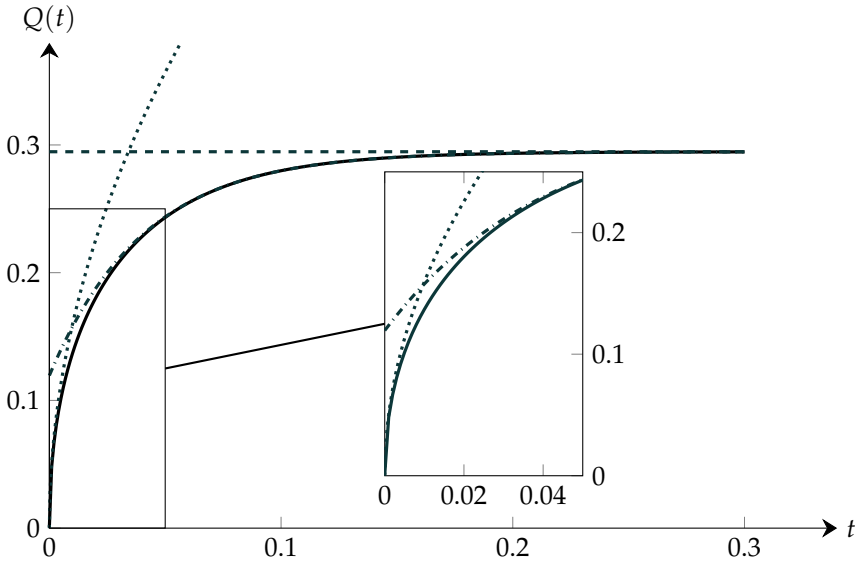


Figure 6. Volumetric flow rate, $Q(t)$, for the startup of Couette flow in a right-angled isosceles triangular channel, with the moving wall along the right leg. The solid curve represents the exact solution, the dashed horizontal line indicates the steady-state limit, the dotted curve shows the short-time asymptotic approximation, and the dash-dotted curve shows the long-time asymptotic approximation.

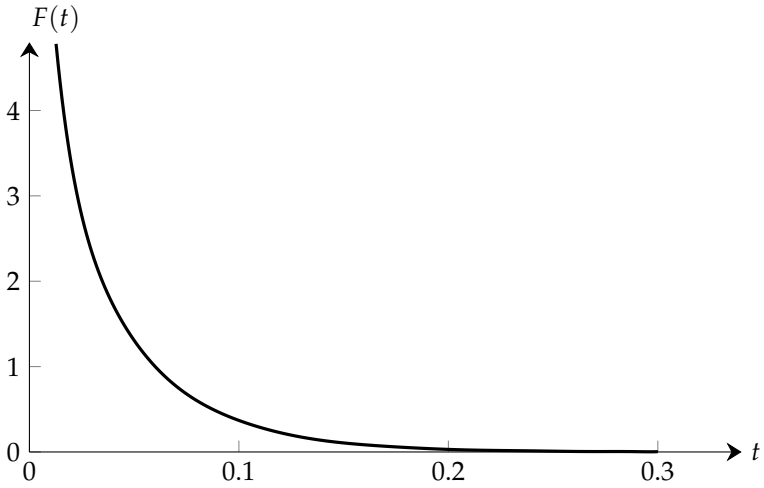


Figure 7. Net rate of viscous momentum transfer from the boundary to the fluid, $F(t)$, for the startup of Couette flow in a right-angled isosceles triangular channel, with the moving wall along the right leg.

4. Rayleigh–Stokes Problem

Before proceeding, it is worth observing that the Rayleigh–Stokes solution may already be inferred from the two single-wall startup problems solved in Section 3. Indeed, the solution generated by the impulsive motion of the left leg is obtained from that for the right leg by reflection about the y-axis, i.e., by replacing x with $-x$. Since Equation (1) is linear and the initial condition (5) is homogeneous, the sum of the hypotenuse-driven solution, the right-leg-driven solution, and its reflected counterpart also satisfies the governing equation and vanishes at $t = 0$. Moreover, on $y = 1$ only the hypotenuse contribution is non-zero, on $y = x$ only the right-leg contribution is non-zero, and on $y = -x$ only the reflected contribution is non-zero. Therefore, this superposition satisfies exactly the Rayleigh–Stokes boundary conditions. This provides a simple physical interpretation of the full motion as the superposition of three single-wall startup flows. For completeness, we now derive the same result directly by an eigenfunction expansion.

A direct derivation is obtained by setting

$$w(x, y, t) = 1 - \tilde{w}(x, y, t), \tag{40}$$

so that Equations (1), (4), and (5) become

$$\frac{\partial \tilde{w}}{\partial t} = \frac{\partial^2 \tilde{w}}{\partial x^2} + \frac{\partial^2 \tilde{w}}{\partial y^2}, \tag{41}$$

with boundary conditions

$$\begin{cases} \tilde{w}(x, y = x, t) = 0, \\ \tilde{w}(x, y = -x, t) = 0, \\ \tilde{w}(x, y = 1, t) = 0, \end{cases} \tag{42}$$

and initial condition

$$\tilde{w}(x, y, 0) = 1. \tag{43}$$

Taking the Laplace transform of Equation (41) with respect to t, and using the initial condition (43), we obtain

$$\frac{\partial^2 \tilde{W}}{\partial x^2} + \frac{\partial^2 \tilde{W}}{\partial y^2} - s\tilde{W} = -1, \tag{44}$$

where

$$\tilde{W}(x, y, s) = \mathscr{L}\{\tilde{w}(x, y, t)\} = \int_0^\infty \tilde{w}(x, y, t)\, \mathrm{e}^{-st}\, \mathrm{d}t. \tag{45}$$

Transforming Equation (42) yields

$$\begin{cases} \tilde{W}(x, y = x, s) = 0, \\ \tilde{W}(x, y = -x, s) = 0, \\ \tilde{W}(x, y = 1, s) = 0. \end{cases} \tag{46}$$

Equation (44) is a non-homogeneous Helmholtz equation with a constant source term, subject to homogeneous Dirichlet conditions. To solve Equations (44) and (46), we use the eigenfunction superposition method.

We seek a solution of the form

$$\tilde{W}(x, y, s) = \sum_{m=1}^{\infty} \sum_{n=1}^{\infty} A_{mn}(s)\, \varphi_{mn}(x, y), \tag{47}$$

where $A_{mn}(s)$ are unknown coefficients, and

$$\varphi_{mn}(x,y) = \cos((\alpha_m+\beta_n)x)\cos((\alpha_m-\beta_n)y) - \cos((\alpha_m-\beta_n)x)\cos((\alpha_m+\beta_n)y), \quad (48)$$

are eigenfunctions of the Helmholtz equation

$$\frac{\partial^2\varphi_{mn}}{\partial x^2} + \frac{\partial^2\varphi_{mn}}{\partial y^2} + \lambda_{mn}^2\varphi_{mn} = 0, \quad (49)$$

which vanish on the boundary of the triangular domain in Figure 1 and, therefore, satisfy the boundary conditions in Equation (46) identically (see, e.g., [45,46]). Here, α_m and β_n are given by Equations (15) and (34), respectively. The corresponding eigenvalues are

$$\lambda_{mn}^2 = 2(\alpha_m^2+\beta_n^2). \quad (50)$$

To clarify the origin of (48), we briefly reinterpret the problem in the rotated and scaled coordinates defined in (23), which transform the physical domain into a unit right triangle. In these coordinates, the eigenfunctions are chosen as combinations of sine products that satisfy the homogeneous Dirichlet conditions on the two legs termwise, while the chosen combination vanishes on the hypotenuse by cancellation. Expression (48) is simply the corresponding form rewritten in the original variables.

The orthogonality of these modes follows from the same geometric construction, as it reduces to the standard orthogonality of sine products on the corresponding square domain. In particular,

$$\int_{-1}^{1}\int_{|x|}^{1}\varphi_{mn}\varphi_{ij}\,\mathrm{d}y\,\mathrm{d}x = \frac{1}{2}\delta_{mi}\delta_{nj}, \quad (51)$$

where δ_{mi} and δ_{nj} denote Kronecker deltas. Moreover,

$$\int_{-1}^{1}\int_{|x|}^{1}\varphi_{mn}\,\mathrm{d}y\,\mathrm{d}x = \frac{2\beta_n}{\alpha_m(\beta_n^2-\alpha_m^2)}. \quad (52)$$

Substitution of (47) into (44) yields

$$\sum_{m=1}^{\infty}\sum_{n=1}^{\infty}\left(s+\lambda_{mn}^2\right)A_{mn}(s)\varphi_{mn} = 1. \quad (53)$$

Projecting (53) onto φ_{mn} over the triangular domain, and using (51) and (52), gives

$$A_{mn}(s) = \frac{4\beta_n}{\alpha_m(\beta_n^2-\alpha_m^2)(s+\lambda_{mn}^2)}. \quad (54)$$

Substituting Equation (54) into Equation (47) and inverting the Laplace transform term by term gives

$$\tilde{w}(x,y,t) = 4\sum_{m=1}^{\infty}\sum_{n=1}^{\infty}\frac{\beta_n}{\alpha_m(\beta_n^2-\alpha_m^2)}\,\varphi_{mn}(x,y)\,\mathrm{e}^{-\lambda_{mn}^2 t}, \quad (55)$$

so that

$$w(x,y,t) = 1 - 4\sum_{m=1}^{\infty}\sum_{n=1}^{\infty}\frac{\beta_n}{\alpha_m(\beta_n^2-\alpha_m^2)}\,\varphi_{mn}(x,y)\,\mathrm{e}^{-\lambda_{mn}^2 t}. \quad (56)$$

The volumetric flow rate is then

$$Q(t) = \int_{-1}^{1}\int_{|x|}^{1} w(x,y,t)\,\mathrm{d}y\,\mathrm{d}x = 1 - 8\sum_{m=1}^{\infty}\sum_{n=1}^{\infty}\frac{\beta_n^2}{\alpha_m^2(\beta_n^2-\alpha_m^2)^2}\mathrm{e}^{-2(\alpha_m^2+\beta_n^2)t}. \quad (57)$$

In a steady state,

$$\lim_{t\to\infty} Q(t) = 1. \tag{58}$$

The limiting behaviour of $Q(t)$ follows directly from the previous two cases. Since the Rayleigh–Stokes solution is obtained by superposing the hypotenuse-driven field and the two reflected right-leg-driven fields, the short-time behaviour is

$$Q(t) \sim \frac{4(1+\sqrt{2})}{\sqrt{\pi}}\, t^{1/2}, \quad t \to 0^+, \tag{59}$$

whereas the long-time behaviour is governed by the slowest-decaying mode $(m, n) = (1, 1)$, yielding

$$1 - Q(t) \sim \frac{512}{9\pi^4} \mathrm{e}^{-\frac{5\pi^2}{2}t}, \quad t \to \infty. \tag{60}$$

Accordingly, the startup again exhibits an initial diffusive regime, followed by exponential relaxation to the steady state.

Figure 8 shows normalised velocity contours for the Rayleigh–Stokes problem at $t = 0.02$, 0.06, and 0.1, from top to bottom. Initially, the highest velocities occur near the moving walls. As time progresses, momentum diffuses inwards due to viscosity, reducing the velocity gradients. The profile becomes progressively more uniform and approaches its steady state, as expected for a diffusion-driven process with no body forces or internal sources.

In view of the superposition argument given at the beginning of this section, the corresponding volumetric flow rate is obtained by adding the hypotenuse contribution to twice that of the right leg. Using the steady limits in Equations (19) and (36), one recovers the value 1, in agreement with (58). The corresponding evolution of $Q(t)$ is shown in Figure 9.

To examine the numerical convergence of (57), Table 3 lists the values of $Q(t)$ obtained by truncating the double series at $m, n = 1, \ldots, N$, for $N = 1, 2, 4$, and 8. The convergence is again rapid for all three times considered. In contrast with the hypotenuse-driven Couette case, the contribution $(m, n) = (1, 1)$ does not vanish here, so that the truncation $N = 1$ already captures the leading transient behaviour. For $t = 0.06$ and $t = 0.10$, the reported digits are recovered with $N = 2$, whereas for $t = 0.02$ one needs $N = 4$. As before, the slower convergence at earlier times reflects the weaker exponential damping, since a larger number of modes still contributes appreciably. A similar truncation pattern is observed in the evaluation of the velocity field. For extra precision, the velocity contours in Figures 2, 5, and 8 were generated using $N = 128$.

Table 3. Convergence of the truncated volumetric flow rate, $Q(t)$, for the Rayleigh–Stokes problem in a right-angled isosceles triangular channel. A dash indicates that the value has converged.

t*/*N	**1**	**2**	**4**	**8**
0.02	0.6435	0.6155	0.6141	–
0.06	0.8671	0.8660	–	–
0.10	0.9505	0.9504	–	–

It follows from (9) and (57) that the net rate of viscous momentum transfer from the boundary to the fluid is

$$F(t) = 16 \sum_{m=1}^{\infty} \sum_{n=1}^{\infty} \frac{\beta_n^2 \left(\alpha_m^2 + \beta_n^2\right)}{\alpha_m^2 \left(\beta_n^2 - \alpha_m^2\right)^2} \mathrm{e}^{-2\left(\alpha_m^2 + \beta_n^2\right)t}. \tag{61}$$

Unlike the impulsively started Couette configurations, the boundary data are compatible at all three vertices, so the resultant force on each wall remains finite for every $t > 0$. The impulsive start nevertheless produces the short-time behaviour

$$F(t) \sim \frac{2\left(1+\sqrt{2}\right)}{\sqrt{\pi t}}, \quad t \to 0^{+}, \tag{62}$$

whereas the long-time decay is governed by the slowest mode,

$$F(t) \sim \frac{1280}{9\pi^2} \mathrm{e}^{-\frac{5\pi^2}{2}t}, \quad t \to \infty. \tag{63}$$

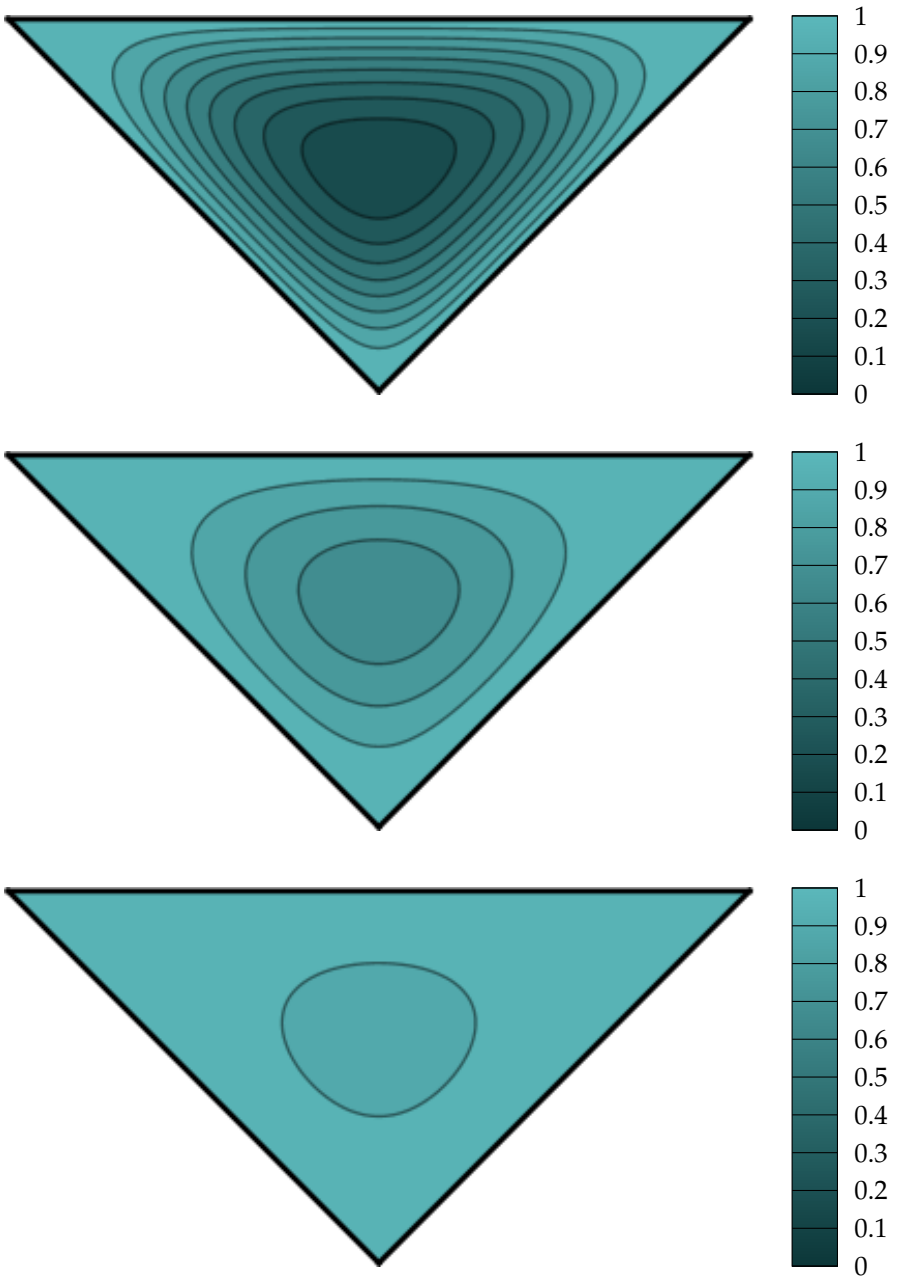


Figure 8. Velocity contours for the Rayleigh–Stokes problem in a right-angled isosceles triangular channel at $t = 0.02$, 0.06, and 0.1 (from top to bottom).

Thus, the viscous loading is again concentrated near startup and then decays monotonically to zero, but without the persistent corner-induced singularities present in the Couette cases, as illustrated in Figure 10.

The local wall shear tractions may also be expressed directly in terms of the eigenfunctions. Using (56), we can observe that, in the Rayleigh–Stokes configuration, the in-

compatibility is purely temporal rather than spatial: all three walls are set into motion simultaneously, so the boundary data remain compatible at the vertices. Accordingly, for every fixed $t > 0$, the series in (56) defines a smooth field up to the boundary, while the limit $t \to 0^+$ is again non-uniform because the fluid is initially at rest. The short-time response is therefore governed by the classical Stokes-layer mechanism along each wall, but without the corner singularities present in the impulsively started Couette configurations.

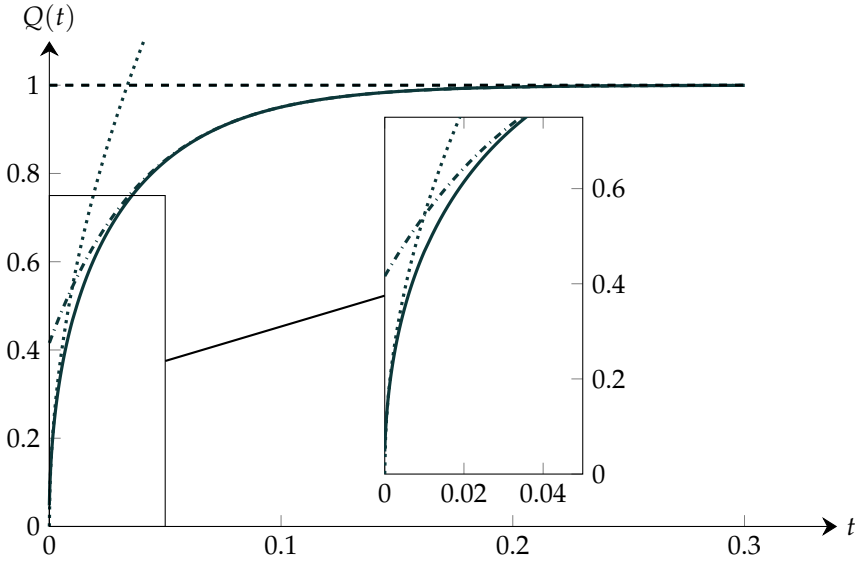


Figure 9. Volumetric flow rate, $Q(t)$, for the Rayleigh–Stokes problem in a right-angled isosceles triangular channel. The solid curve represents the exact solution, the dashed horizontal line indicates the steady-state limit, the dotted curve shows the short-time asymptotic approximation, and the dash-dotted curve shows the long-time asymptotic approximation.

Substitution into (6) yields

$$\tau_{y=1}(x,t) = 4\sum_{m=1}^{\infty}\sum_{n=1}^{\infty}\frac{\beta_n}{\alpha_m(\beta_n^2-\alpha_m^2)}\left.\frac{\partial\varphi_{mn}}{\partial y}\right|_{y=1} \mathrm{e}^{-2\left(\alpha_m^2+\beta_n^2\right)t}, \tag{64a}$$

$$\tau_{y=x}(x,t) = \frac{4}{\sqrt{2}}\sum_{m=1}^{\infty}\sum_{n=1}^{\infty}\frac{\beta_n}{\alpha_m(\beta_n^2-\alpha_m^2)}\left.\left(\frac{\partial\varphi_{mn}}{\partial x}-\frac{\partial\varphi_{mn}}{\partial y}\right)\right|_{y=x} \mathrm{e}^{-2\left(\alpha_m^2+\beta_n^2\right)t}, \tag{64b}$$

$$\tau_{y=-x}(x,t) = -\frac{4}{\sqrt{2}}\sum_{m=1}^{\infty}\sum_{n=1}^{\infty}\frac{\beta_n}{\alpha_m(\beta_n^2-\alpha_m^2)}\left.\left(\frac{\partial\varphi_{mn}}{\partial x}+\frac{\partial\varphi_{mn}}{\partial y}\right)\right|_{y=-x} \mathrm{e}^{-2\left(\alpha_m^2+\beta_n^2\right)t}. \tag{64c}$$

These tractions are finite for every $t > 0$, in contrast with the impulsively started Couette configurations. In the present problem, one also finds that

$$\tau_{y=1}(\pm 1,t) = 0, \quad \tau_{y=x}(0,t) = \tau_{y=x}(1,t) = 0, \quad \tau_{y=-x}(-1,t) = \tau_{y=-x}(0,t) = 0, \tag{65}$$

for every $t > 0$. Thus, the wall shear is distributed smoothly along each side, rather than being concentrated at the corners.

With the present sign convention, the tractions are negative, which simply reflects that the fluid exerts a retarding viscous shear on walls moving in the positive axial direction. At short times, each smooth wall segment is locally equivalent to the classical Rayleigh–Stokes problem for an impulsively started flat plate [1], so that

$$\tau \sim -\frac{1}{\sqrt{\pi t}}, \quad t \to 0^+, \tag{66}$$

uniformly on compact subsets away from the vertices. At long times, the tractions decay exponentially with the same leading rate as the global load. In particular,

$$\tau_{y=1}(x,t) \sim -\frac{16}{3\pi}\left[3\cos\left(\frac{\pi x}{2}\right)+\cos\left(\frac{3\pi x}{2}\right)\right]e^{-\frac{5\pi^2}{2}t}, \quad t\to\infty, \tag{67}$$

$$\tau_{y=x}(x,t) \sim -\frac{32\sqrt{2}}{3\pi}\left[\sin(\pi x)+\frac{1}{2}\sin(2\pi x)\right]e^{-\frac{5\pi^2}{2}t}, \quad t\to\infty, \tag{68}$$

with $\tau_{y=-x}(x,t) \sim \tau_{y=x}(-x,t)$. This is consistent with the approach to the uniform steady state $w=1$, for which all shear tractions vanish.

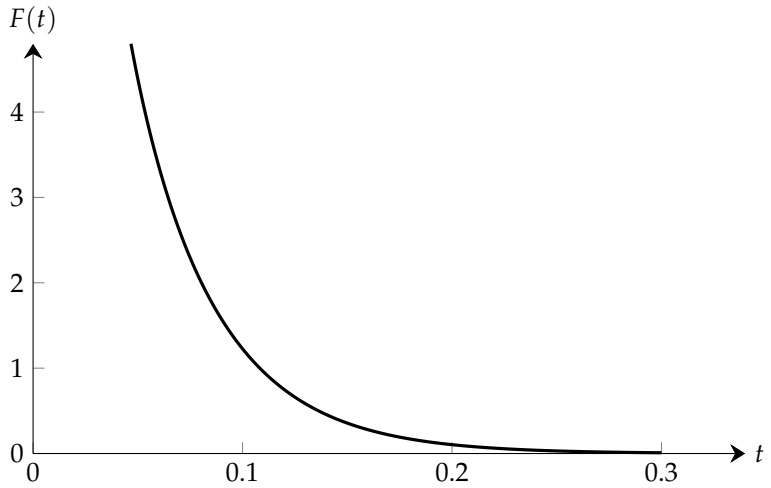


Figure 10. Net rate of viscous momentum transfer from the boundary to the fluid, $F(t)$, for the Rayleigh–Stokes problem in a right-angled isosceles triangular channel.

5. Comparison with Classical Startup Flows

To place the present triangular solutions in context, we compare them with previously known exact startup solutions in canonical separable geometries. For startup Couette flow, the natural benchmark is the square channel with one moving wall, while for the Rayleigh–Stokes problem useful benchmarks are provided by the corresponding square- and circular-channel solutions. These reference cases were studied, for example, by Erdoğan [23] for rectangular and square channels, and by Wu and Wu [22] for the circular Rayleigh–Stokes problem.

Since the triangular cross-section considered here has unit area, the square and the circle used for comparison were also chosen to have unit area. Accordingly, the square is taken as $[0,1]\times[0,1]$, while the circular cross-section has the radius $1/\sqrt{\pi}$. The curves are therefore compared at a fixed area, so that the differences seen in the figures reflect only the geometry and the boundary forcing.

For completeness, we record the exact expressions used to generate the comparison curves. For the Rayleigh–Stokes problem in the square, the separation of variables gives

$$Q(t) = 1 - 4\sum_{m=1}^{\infty}\sum_{n=1}^{\infty}\frac{e^{-4\left(\alpha_m^2+\alpha_n^2\right)t}}{\alpha_m^2\alpha_n^2}. \tag{69}$$

The corresponding startup Couette flow in the square, with one moving wall and the other three at rest, follows immediately by linearity and symmetry. Indeed, the sum of the four single-wall startup Couette solutions is precisely the square Rayleigh–Stokes solution, and all four contributions have the same volumetric flow rate. Therefore,

$$Q(t) = \frac{1}{4} - \sum_{m=1}^{\infty} \sum_{n=1}^{\infty} \frac{\mathrm{e}^{-4\left(\alpha_m^2+\alpha_n^2\right)t}}{\alpha_m^2 \alpha_n^2}. \tag{70}$$

For the Rayleigh–Stokes problem in the circle, radial symmetry yields

$$Q(t) = 1 - 4 \sum_{n=1}^{\infty} \frac{\mathrm{e}^{-\pi j_{0,n}^2 t}}{j_{0,n}^2}, \tag{71}$$

where $j_{0,n}$ denotes the n-th positive zero of the Bessel function J_0 of the first kind.

Figure 11 compares the volumetric flow rate for startup Couette flow in the right-angled isosceles triangular channel with that in a square channel. All three curves exhibit the same broad pattern—namely, an initial diffusive growth, followed by relaxation towards a steady Couette state. The main geometric effect is already visible at short times: the triangular channel driven along the hypotenuse rises most rapidly, the same channel driven along one leg rises more slowly, and the square channel yields the weakest initial response. This ordering is fully consistent with the short-time behaviour derived earlier, since the leading contribution depends on the length of the moving boundary. For unit area, the hypotenuse is longer than a leg, and a leg is longer than the moving side of the square. At later times, the separation between the curves is controlled by the full eigenvalue spectrum of each cross-section, so that the approach to the steady state remains geometry-dependent throughout the transient.

The steady limits are also instructive. For the two triangular configurations, the limiting values are consistent with (19) and (36), while (70) gives

$$Q_\infty = \lim_{t\to\infty} Q(t) = \frac{1}{4} \tag{72}$$

for the square channel. Thus, the three Couette curves approach distinct steady levels, with the hypotenuse-driven triangular flow attaining the largest value and the square channel the smallest.

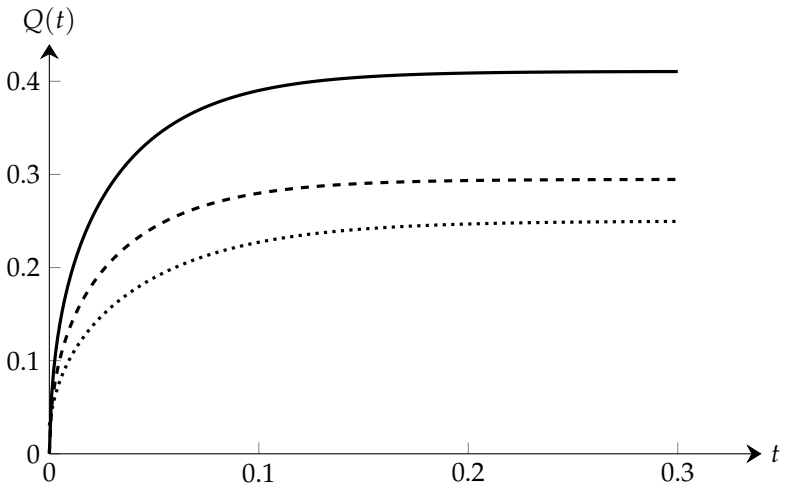


Figure 11. Volumetric flow rate, $Q(t)$, for startup Couette flow. The solid curve corresponds to the right-angled isosceles triangular channel with the moving wall along the hypotenuse, the dashed curve to the same channel with the moving wall along one leg, and the dotted curve to a square channel with one moving wall.

Figure 12 shows the corresponding comparison for the Rayleigh–Stokes problem. In this case, the three curves tend to the same limit, since the final state is uniform axial motion throughout the cross-section. The short-time ordering is again clear: the triangular

channel rises fastest, the square channel follows, and the circular channel exhibits the slowest initial growth. This is consistent with the short-time law obtained earlier, according to which the leading contribution depends on the total moving perimeter. For unit area, the triangle has the largest perimeter, the square an intermediate one, and the circle the smallest. The same ordering is therefore expected at early times and remains visible throughout the transient shown in the figure. At later times, as in the Couette case, the remaining differences are governed by the spectral properties of the corresponding cross-sections. The triangular channel thus fits naturally within the classical startup-flow picture, while making explicit how a physically non-separable geometry modifies both the transient amplitude and the rate of relaxation.

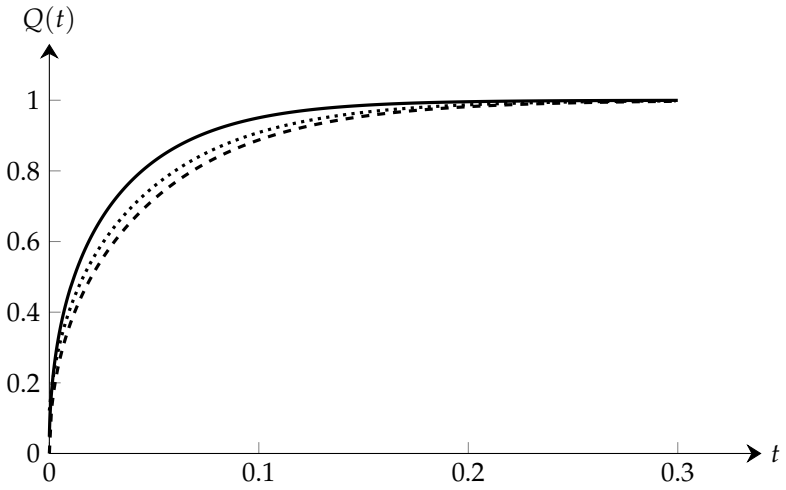


Figure 12. Volumetric flow rate, $Q(t)$, for the Rayleigh–Stokes problem. The solid curve corresponds to the right-angled isosceles triangular channel, the dotted curve to a square channel, and the dashed curve to a circular channel.

6. Conclusions

Analytical studies of unsteady Stokes flows form a substantial body of literature, particularly for external flows, immersed bodies, and formulations based on fundamental solutions or singularity methods [47–51]. In contrast, exact solutions for startup flows in confined geometries that are non-separable in their physical form remain relatively scarce.

Exact transient series solutions have been obtained for three impulsively driven startup flows in a right-angled isosceles triangular channel: two Couette configurations, and the Rayleigh–Stokes case. Although the triangular cross-section does not admit standard separation of variables in its physical form, its reflection symmetries make it possible to reduce the problem to separable Helmholtz formulations and thereby construct explicit eigenfunction expansions. This provides a rare exact treatment of startup viscous motion in a closed non-separable geometry.

The three configurations exhibit clearly distinct transient responses. In the Couette problem, motion of the hypotenuse produces a stronger flow than motion of one leg, both at early times and in the steady limit, because momentum is injected through a longer moving boundary. In the Rayleigh–Stokes problem, the boundary data are compatible at the vertices, so the resultant wall forces remain finite for every $t > 0$, in contrast with the Couette cases, where corner singularities persist on the individual walls. The derived expressions for the velocity field, the volumetric flow rate, and the net viscous momentum transfer make these differences fully explicit.

The short- and long-time asymptotics also clarify the physical structure of the startup process. At early times, the motion is confined to thin viscous layers near the moving

boundaries, and the leading growth of $Q(t)$ is determined by the total length of the impulsively driven wall, in agreement with the local reduction to Stokes' first problem away from the vertices [1,2]. At late times, the approach to equilibrium is governed by the slowest-decaying eigenmode, while the steady Couette limits recover the expected confined-wall behaviour of the classical startup plane Couette problem [3]. The comparison with equal-area square and circular channels shows that, in the Rayleigh–Stokes problem, the triangular geometry produces the fastest initial rise, while in startup Couette flow the ordering depends on which wall is set into motion.

From an applied viewpoint, the present solutions furnish exact benchmark results for transient motion in non-circular passages. They may be useful for validating numerical schemes, assessing reduced-order approximations, and interpreting transient transport and wall loading in geometries for which closed-form results are scarce. Natural extensions include other triangular startup problems, pressure-driven unsteady flows, and related diffusion-type problems in polygonal domains with comparable symmetry. More broadly, once the relevant spectral data are available, the same framework may be adapted to other linear Helmholtz-type problems in the spirit discussed by Moon and Spencer [52].

Author Contributions: V.C.d.S.: Conceptualization, methodology, software, validation, formal analysis, data curation, writing—original draft, funding acquisition. A.v.B.L.: Conceptualization, methodology, software, validation, formal analysis, writing—review and editing, supervision. All authors have read and agreed to the published version of the manuscript.

Funding: V.C.d.S. Silva would like to express his gratitude for the financial support provided by the Fundação de Apoio à Pesquisa do Distrito Federal (N° FAPDF: 145/2026, Edital No. 01/2026—FAPDF Publica).

Data Availability Statement: No new data were created or analysed in this study.

Conflicts of Interest: The authors declare no conflicts of interest.

Nomenclature

Unless otherwise stated, all variables are dimensionless. The reference scales are L for length, V for velocity, and L^2/ν for time.

Roman symbols

$A_{mn}(s)$	Expansion coefficients
$F(t)$	Momentum-transfer rate
J_0	Bessel function of the first kind of order zero
$j_{0,n}$	n-th positive zero of J_0
L	Characteristic length [m]
N	Truncation level
$Q(t)$	Volumetric flow rate
s	Laplace variable
t	Time
t'	Transformed time
V	Wall velocity [$\mathrm{m} \cdot \mathrm{s}^{-1}$]
$W(x, y, s)$	Laplace transform of w
$W(x', y', s)$	Laplace transform of w in transformed coordinates
$w(x, y, t)$	Axial velocity
$w(x', y', t')$	Axial velocity in transformed coordinates
x, y	Cartesian coordinates
x', y'	Rotated coordinates

Greek symbols

α_m	Spectral parameter
β_n	Spectral parameter

δ_{mi}, δ_{nj}	Kronecker delta
λ_{mn}	Eigenvalues
μ	Dynamic viscosity [Pa · s]
ν	Kinematic viscosity [$m^2 \cdot s^{-1}$]
$\tau_{y=1}(x,t)$	Wall shear traction on $y = 1$
$\tau_{y=x}(x,t)$	Wall shear traction on $y = x$
$\tau_{y=-x}(x,t)$	Wall shear traction on $y = -x$
$\tilde{W}(x,y,s)$	Laplace transform of $\tilde{w}$
$\tilde{w}(x,y,t)$	Auxiliary velocity field
$\varphi_{mn}(x,y)$	Eigenfunctions
Operators and indices	
∇^2	Laplacian
$\mathscr{L}\{\cdot\}$	Laplace transform
$\partial/\partial n$	Outward normal derivative
m, n, i, j	Mode indices

References

1. Stokes, G.G. On the effect of the internal friction of fluids on the motion of pendulums. *Trans. Camb. Philos. Soc.* **1851**, *9*, 8–106.
2. Strutt, J.W. On the motion of solid bodies through viscous liquid. *Philos. Mag.* **1911**, *21*, 697–711. [CrossRef]
3. Papanastasiou, T.C.; Georgiou, G.C.; Alexandrou, A.N. *Viscous Fluid Flow*, 2nd ed.; CRC Press: Boca Raton, FL, USA, 2000.
4. Stewartson, K. On the impulsive motion of a flat plate in a viscous fluid. *Q. J. Mech. Appl. Math.* **1951**, *4*, 182–198. [CrossRef]
5. MacDonald, D.A. The Rayleigh Problem for a Two-Layer Fluid. *Q. J. Mech. Appl. Math.* **1966**, *19*, 197–211. [CrossRef]
6. Tanner, R.I. Note on the Rayleigh Problem for a Visco-Elastic Fluid. *Z. Angew. Math. Phys.* **1962**, *13*, 573–580. [CrossRef]
7. Fetecau, C.; Fetecau, C. The first problem of Stokes for an Oldroyd-B fluid. *Int. J. Non. Linear Mech.* **2003**, *38*, 1539–1544. [CrossRef]
8. Preziosi, L.; Joseph, D.D. Stokes' first problem for viscoelastic fluids. *J. Non-Newton. Fluid Mech.* **1987**, *25*, 239–259. [CrossRef]
9. Khan, Z.H.; Khan, W.A.; Ibrahim, S.M.; Mabood, F.; Huang, Z. Effects of thermal boundary conditions on Stokes' second problem. *Results Phys.* **2024**, *60*, 107662. [CrossRef]
10. Salah, F.; Abdul Aziz, Z.; Ling Chuan Ching, D. New exact solution for Rayleigh–Stokes problem of Maxwell fluid in a porous medium and rotating frame. *Results Phys.* **2011**, *1*, 9–12. [CrossRef]
11. Erdoğan, M.E. On the unsteady unidirectional flows generated by impulsive motion of a boundary or sudden application of a pressure gradient. *Int. J. Eng. Sci.* **2002**, *40*, 1605–1625. [CrossRef]
12. Bandelli, S.; Rajagopal, K.R. Start-up flows of second grade fluids in domains with one finite dimension. *J. Non-Newton. Fluid Mech.* **1995**, *58*, 215–228. [CrossRef]
13. Wenchang, T.; Wenxiao, P.; Mingyu, X. A note on unsteady flows of a viscoelastic fluid with the fractional Maxwell model between two parallel plates. *Int. J. Non-Linear Mech.* **2003**, *38*, 645–650. [CrossRef]
14. Vieru, D.; Zafar, A. Some Couette flows of a Maxwell fluid with wall slip condition. *Appl. Math. Inf. Sci.* **2013**, *7*, 209–219. [CrossRef]
15. Jordan, P.M.; Puri, P. Stokes' first problem for a Rivlin–Ericksen fluid of second grade in a porous half-space. *Int. J. Non-Linear Mech.* **2003**, *38*, 1019–1025. [CrossRef]
16. Balan, C. Note on the start-up of Couette flow for viscoelastic fluids. *Phys. Fluids* **2023**, *35*. [CrossRef]
17. Jha, B.K.; Danjuma, Y.J. Impact of Variable Viscosity on Unsteady Couette Flow. *Heat Transf.* **2025**, *54*, 2032–2048. [CrossRef]
18. Shahid, A.; Zhou, Z.; Hassan, M.; Bhatti, M.M. Computational Study of Magnetized Blood Flow in the Presence of Gyrotactic Microorganisms Propelled through a Permeable Capillary in a Stretching Motion. *Int. J. Multiscale Comput. Eng.* **2018**, *16*, 409–426. [CrossRef]
19. Vinod, Y.; Raghunatha, K.R.; Nagappanavar, S.N.; Nazarova, N.; Gupta, M.; Sangamesh. Boundary layer flow of a non-Newtonian fluid over an exponentially stretching sheet with the presence of a heat source/sink. *Partial Differ. Equ. Appl. Math.* **2025**, *13*, 101111. [CrossRef]
20. Crane, L.J. Flow Past a Stretching Plate. *Z. Angew. Math. Phys.* **1970**, *21*, 645–647. [CrossRef]
21. Gupta, P.S.; Gupta, A.S. Heat and Mass Transfer on a Stretching Sheet with Suction or Blowing. *Can. J. Chem. Eng.* **1977**, *55*, 744–746. [CrossRef]
22. Wu, J.C.; Wu, T.Y.T. Generalized Rayleigh's Problem in Viscous Flows. *Q. J. Mech. Appl. Math.* **1967**, *20*, 393–427. [CrossRef]
23. Erdoğan, M.E. On the flows produced by sudden application of a constant pressure gradient or by impulsive motion of a boundary. *Int. J. Non-Linear Mech.* **2003**, *38*, 781–797. [CrossRef]
24. Silva, V.C.; Lustosa, B.P.; Lopes, A.B. Startup of Poiseuille flow in triangular ducts. *Z. Angew. Math. Phys.* **2025**, *76*, 241. [CrossRef]

25. Nadeem, S.; Asghar, S.; Hayat, T.; Hussain, M. The Rayleigh Stokes problem for rectangular pipe in Maxwell and second grade fluid. *Meccanica* **2008**, *43*, 495–504. [CrossRef]
26. Xia, Y.; Su, Z.; Zhang, Y.; Li, L. A general form of starting solutions of linear viscoelastic fluids for Couette flow. *Phys. Fluids* **2025**, *37*, 033107. [CrossRef]
27. Au, V.V.; Caraballo, T. A Mixed Nonlinear Time-Fractional Rayleigh–Stokes Equation. *Discret. Contin. Dyn. Syst. S* **2023**, *16*, 2589–2612. [CrossRef]
28. He, J.W.; Zhou, Y.; Peng, L.; Ahmad, B. On Well-Posedness of Semilinear Rayleigh–Stokes Problem with Fractional Derivative on $\mathbb{R}^N$. *Adv. Nonlinear Anal.* **2022**, *11*, 580–597. [CrossRef]
29. Ashurov, R.; Mukhiddinova, O.; Umarov, S. A Non-Local Problem for the Fractional-Order Rayleigh–Stokes Equation. *Fractal Fract.* **2023**, *7*, 490. [CrossRef]
30. Long, L.D.; Moradi, B.; Nikan, O.; Avazzadeh, Z.; Lopes, A.M. Numerical Approximation of the Fractional Rayleigh–Stokes Problem Arising in a Generalised Maxwell Fluid. *Fractal Fract.* **2022**, *6*, 377. [CrossRef]
31. Abd-Elhameed, W.M.; Al-Sady, A.M.; Alqubori, O.M.; Atta, A.G. Numerical Treatment of the Fractional Rayleigh–Stokes Problem Using Some Orthogonal Combinations of Chebyshev Polynomials. *AIMS Math.* **2024**, *9*, 25457–25481. [CrossRef]
32. Safari, F.; Feng, X. The Development of a Mesh-Free Technique for the Fractional Model of the Inverse Problem of the Rayleigh–Stokes Equation with Additive Noise. *Fractal Fract.* **2025**, *9*, 551. [CrossRef]
33. Tsangaris, S.; Vlachakis, N.W. Exact solution of the Navier–Stokes equations for the oscillating flow in a duct of a cross-section of right-angled isosceles triangle. *Z. Angew. Math. Phys. (ZAMP)* **2003**, *54*, 1094–1100. [CrossRef]
34. Lopes, A.B.; Far, M.E.F.; Da Silva, V.C. Revisiting Darcy–Brinkman Flow Through an Elliptic Tube. *Transp. Porous Media* **2026**, *153*, 13. [CrossRef]
35. Sun, X.; Wang, S.; Zhao, M. Oscillatory flow of Maxwell fluid in a tube of isosceles right triangular cross section. *Phys. Fluids* **2019**, *31*, 123101. [CrossRef]
36. Ershkov, S.V. Exact solution of Helmholtz equation for the case of non-paraxial Gaussian beams. *J. King. Saud. Univ. Sci.* **2015**, *27*, 198–203. [CrossRef]
37. Venegas, R.; Boutin, C. Acoustics of permeable media with active internal heat sources. *Phys. Fluids* **2025**, *37*, 077182. [CrossRef]
38. Wang, C.Y. *Essential Analytic Heat Transfer*; Springer Nature: Cham, Switzerland, 2024.
39. Joachimiak, M.; Frąckowiak, A. Analysis of heat transfer in a cylinder being treated in a gas nitriding furnace using a new inverse problem solving method. *Energy* **2025**, *333*, 137318. [CrossRef]
40. Zhang, Z.; He, G.; Gou, Y.; Luan, Z.; Liu, S.; He, R. Wavelength manipulation in shallow water via space transformation method. *Phys. Fluids* **2023**, *35*, 117108. [CrossRef]
41. Wang, C.Y. Sloshing in Regular Polygonal Basins—Frequencies, Modes, and Tileability. *J. Fluids Eng.* **2020**, *142*, 064502. [CrossRef]
42. Núñez-Fernández, Y.; Trallero-Giner, C.; Buchleitner, A. Liquid surface waves in parabolic tanks. *Phys. Fluids* **2008**, *20*, 117106. [CrossRef]
43. Wang, C.Y.; Wang, C.M. *Structural Vibration: Exact Solutions for Strings, Membranes, Beams, and Plates*; CRC Press: Boca Raton, FL, USA, 2014. [CrossRef]
44. Polyanin, A.D. *Handbook of Exact Solutions to Mathematical Equations*; Advances in Applied Mathematics; Chapman and Hall/CRC: Boca Raton, FL, USA, 2024. [CrossRef]
45. Nuttall, H. Torsion of Uniform Rods With Particular Reference to Rods of Triangular Cross Section. *J. Appl. Mech.* **2021**, *19*, 554–557. [CrossRef]
46. Silva, V.C.; Moreira, G.G.; Lopes, A.B.L.; Alassar, R.S.M. Poiseuille flow through parabolic segment and lens-shaped ducts. *IMA J. Appl. Math.* **2025**, *90*, 347–369. [CrossRef]
47. Pozrikidis, C. A singularity method for unsteady linearized flow. *Phys. Fluids A Fluid Dyn.* **1989**, *1*, 1508–1520. [CrossRef]
48. Mauri, R.; Rubinstein, J. On the propagator of the Stokes equation and a dynamical definition of viscosity. *Chem. Eng. Commun.* **1996**, *148*, 385–390. [CrossRef]
49. Fouxon, I.; Leshansky, A. Fundamental solution of unsteady Stokes equations and force on an oscillating sphere near a wall. *Phys. Rev. E* **2018**, *98*, 063108. [CrossRef]
50. Hsiao, C.H.; Young, D.L. The singularity method in unsteady Stokes flow: Hydrodynamic force and torque around a sphere in time-dependent flows. *J. Fluid Mech.* **2019**, *863*, 1–31. [CrossRef]
51. Procopio, G.; Biagioni, V.; Giona, M. The resistance of an arbitrary body in confined unsteady Stokes flow. *Fluids* **2024**, *9*, 260. [CrossRef]
52. Moon, P.; Spencer, D.E. *Field Theory Handbook: Including Coordinate Systems, Differential Equations and Their Solutions*; Springer: Berlin/Heidelberg, Germany, 1988.

Disclaimer/Publisher's Note: The statements, opinions and data contained in all publications are solely those of the individual author(s) and contributor(s) and not of MDPI and/or the editor(s). MDPI and/or the editor(s) disclaim responsibility for any injury to people or property resulting from any ideas, methods, instructions or products referred to in the content.